NUMERICAL SIMULATION OF RECEPTIVITY AND STABILITY OF A SUPERSONIC BOUNDARY LAYER

V.G. Soudakov, I.V. Egorov, A.V. Fedorov, A.V. Novikov
TsAGI, 140180, Russia, Moscow region, Zhukovsky, Zhukovsky str., 1

Keywords: *stability, supersonic boundary layer, flow control*

Abstract

Two-dimensional direct numerical simulations (DNS) of receptivity and stability of a supersonic boundary layer over a flat plate, cone, compression corner and wavy wall are carried out for the cases of solid and porous wall. It is shown that proper designed porous coating and wavy surface can lead to decreasing of disturbances in the boundary layer that may increase laminar run substantially.

1 Introduction

Prediction of laminar-turbulent transition is important for aerothermal design and drag calculations of high-speed vehicles. Premature transition may be critical because it reduces propulsion system efficiency, increases viscous drag (that can be more than 30% of the total drag), as well as degrades aerodynamic control surfaces and reaction control system performance. Because of these issues, strategies for achieving economically viable aerospace systems require laminar flow control (LFC) concepts that substantially delay transition.

In the two-dimensional high-speed boundary layer, the first and second modes [1] are dominant instabilities at sufficiently small pressure gradients (when cross-flow and Görtler vortices are stable). First mode is associated with Tollmien–Schlichting waves, while the second mode is one of the modes related to trapped acoustic waves [1]. The first mode can be stabilized by the wall cooling, suction, and favorable pressure gradient [2]. The second mode begins to dominate in the boundary layer at sufficiently high local Mach numbers (approximately M>4). As contrasted to the first mode, the wall cooling destabilizes the second mode. Since the surface temperature of typical high-speed vehicles is essentially lower than the adiabatic wall temperature, the first-mode instability is suppressed naturally while the second mode grows faster and can lead to early laminar-turbulent transition. This indicates that high-speed laminar-flow-control concepts should address the second-mode instability.

Because the second mode represents high frequency (ultrasonic) acoustic waves, Fedorov et al. [3] assumed that a passive ultrasonically absorptive coating (UAC) may stabilize the second mode and, at the same time, be aerodynamically smooth. This hypothesis was confirmed by theoretical studies based on the linear stability theory (LST) and experiments in ITAM (Novosibirsk, Russia) [4].

Herein this concept is investigated by means of DNS method described in [5]. Numerical solutions are obtained using the implicit second-order finite-volume TVD (total variation diminishing) method. At first, the steady-state solution of Navier-Stokes equations, which satisfies the undisturbed free-stream boundary conditions, is calculated to provide the mean laminar flow. For investigation of the boundary-layer receptivity and stability, initial disturbances are induced by the boundary condition. The following geometries are considered: flat plate, sharp cone, compression corner, flat plate with wavy wall.

2 Problem Formulation

Viscous unsteady compressible flows are governed by Navier-Stokes equations. For two-

dimensional flows, these equations are written in the conservative nondimensional form

$$\frac{\partial \mathbf{Q}}{\partial t}+\frac{\partial \mathbf{E}}{\partial \xi}+\frac{\partial \mathbf{G}}{\partial \eta}=0$$

where (ξ,η) is a curvilinear coordinate system, $x=x(\xi,\eta)$, $y=y(\xi,\eta)$ are Cartesian coordinates, $\mathbf{Q}$ is vector of dependent variables, $\mathbf{E}$ and $\mathbf{G}$ are flux vectors in the (ξ,η) coordinate system. These vectors are expressed in terms of the corresponding vectors $\mathbf{Q}_c,\mathbf{E}_c,\mathbf{G}_c$ in Cartesian coordinate system as

$$\mathbf{Q}=J\mathbf{Q}_c$$
$$\mathbf{E}=J\left(\mathbf{E}_c\frac{\partial \xi}{\partial x}+\mathbf{G}_c\frac{\partial \xi}{\partial y}\right)$$
$$\mathbf{G}=J\left(\mathbf{E}_c\frac{\partial \eta}{\partial x}+\mathbf{G}_c\frac{\partial \eta}{\partial y}\right)$$

where $J=\det\left\|\partial(x,y)/\partial(\xi,\eta)\right\|$ is the transformation Jacobian. Cartesian vector components for two-dimensional Navier–Stokes equations are

$$\mathbf{Q}_c=\begin{bmatrix}\rho\\ \rho u\\ \rho v\\ e\end{bmatrix}$$

$$\mathbf{E}_c=\begin{bmatrix}\rho u\\ \rho u^2+p-\dfrac{1}{\mathrm{Re}_\infty}\tau_{xx}\\ \rho uv-\dfrac{1}{\mathrm{Re}_\infty}\tau_{xy}\\ \rho uH-\dfrac{1}{\mathrm{Re}_\infty}\left(\begin{array}{c}u\tau_{xx}+v\tau_{xy}+\\ +\dfrac{\mu}{\mathrm{Pr}(\gamma-1)\mathrm{M}_\infty^2}\dfrac{\partial T}{\partial x}\end{array}\right)\end{bmatrix}$$

$$\mathbf{G}_c=\begin{bmatrix}\rho v\\ \rho uv-\dfrac{1}{\mathrm{Re}_\infty}\tau_{xy}\\ \rho v^2+p-\dfrac{1}{\mathrm{Re}_\infty}\tau_{yy}\\ \rho vH-\dfrac{1}{\mathrm{Re}_\infty}\left(\begin{array}{c}u\tau_{xy}+v\tau_{yy}+\\ +\dfrac{\mu}{\mathrm{Pr}(\gamma-1)\mathrm{M}_\infty^2}\dfrac{\partial T}{\partial y}\end{array}\right)\end{bmatrix}$$

Here, ρ is density; u,v are Cartesian components of the velocity vector $\mathbf{V}$; p is pressure; T is temperature; $e=\dfrac{p}{\gamma-1}+\dfrac{1}{2}\rho\left(u^2+v^2\right)$ is total energy; $H=\dfrac{T}{(\gamma-1)M_\infty^2}+\dfrac{1}{2}\left(u^2+v^2\right)$ is total specific enthalpy; τ is stress tensor with components

$$\tau_{xx}=\mu\left(-\frac{2}{3}div\mathbf{V}+2\frac{\partial u}{\partial x}\right)$$
$$\tau_{xy}=\mu\left(\frac{\partial u}{\partial y}+\frac{\partial v}{\partial x}\right)$$
$$\tau_{yy}=\mu\left(-\frac{2}{3}div\mathbf{V}+2\frac{\partial v}{\partial y}\right)$$

The fluid is a perfect gas with the specific heat ratio $\gamma=1.4$ and Prandtl number $\mathrm{Pr}=0.72$. The system of equations is closed by state equation $p=\rho T/\left(\gamma\mathrm{M}_\infty^2\right)$. The viscosity-temperature dependence is approximated by the power law $\mu^*/\mu_\infty^*=\left(T^*/T_\infty^*\right)^{0.7}$. Hereafter asterisks denote dimensional variables. The second viscosity is assumed to be zero.

Numerical studies are carried out for supersonic flow at the free-stream Mach number M_∞ and the Reynolds number $\mathrm{Re}_\infty=\rho_\infty^*U_\infty^*L^*/\mu_\infty^*$, where ρ_∞^* – free-stream density, U_∞^* – free-stream velocity, L^* – characteristic length. Flow variables are made nondimensional using the steady-state free-stream parameters as $(u,v)=(u^*,v^*)/U_\infty^*$, $p=p^*/(\rho_\infty^*U_\infty^{*2})$, $\rho=\rho/\rho_\infty^*$, $T=T^*/T_\infty^*$. The

nondimensional coordinates and time are $(x,y)=(x^*,y^*)/L^*$, $t=t^*U_\infty^*/L^*$.

Details on the problem formulation and governing equations are given in [5]. The problem is solved numerically using the implicit second-order finite-volume method described in [5]. Two-dimensional Navier-Stokes equations are approximated by TVD shock-capturing scheme. The shock-capturing scheme allows for modeling of the disturbance dynamics in the complex flows with different shock waves. Nevertheless this computational scheme damps physical waves, especially near the peaks and valleys. The numerical dissipation can be suppressed using sufficiently fine computational grids. DNS of disturbances generated by a local periodic suction-blowing in the boundary layer on a flat plate was carried out in [5] and it was shown that this method is appropriate for modeling of the boundary-layer instability. Namely, the calculated second-mode growth rate agreed well with that predicted by LST.

3 Porous coatings

3.1 Flat plate

Calculations are carried out for supersonic flow over a flat plate with sharp leading edge at the free-stream Mach number $M_\infty=6$ and Reynolds number $Re_\infty=2\times10^6$ (based on the plate length L^*). The computational domain is a rectangle with its bottom side corresponding to the plate surface. For the solid wall case, the no-slip boundary conditions are imposed on the plate surface. The wall temperature corresponds to the adiabatic condition for the steady-state solution. On the outflow boundary, the flow variables are extrapolated using the linear approximation. On the inflow and upper boundaries, the boundary conditions correspond to the free stream quantities. The computational grid has 2001×301 nodes. The grid nodes are clustered in the boundary layer and in the leading-edge region.

For modeling of the boundary-layer instability, initial disturbances are induced by a local periodic suction-blowing in the leading-edge vicinity. The mass flow on the plate surface is given by

$$q_w(x,t)=\frac{\rho_w^*v_w^*}{\rho_\infty^*U_\infty^*}= \\ =\varepsilon\sin\left(2\pi\frac{x-x_1}{x_2-x_1}\right)\sin(\omega t) \\ x_1\le x\le x_2,\ t>0 \qquad (1)$$

where ε is forcing amplitude; $x_1=0.0358$, $x_2=0.0495$ are boundaries of the local suction-blowing region; the angular velocity $\omega=\omega^*L^*/U_\infty^*=260$ corresponds to high-frequency disturbances including unstable second-mode waves. The amplitude $\varepsilon=6\times10^{-4}$ was chosen small enough to ensure validity of the linear approximation and compare DNS results with LST. In the unsteady problem, the wall temperature corresponds to adiabatic wall, $T_w(x,t)=T_{ad}(x)$; i.e., the temperature disturbances on the wall are zero.

For modeling of the UAC effect, the boundary condition on the porous wall is formulated using the analytical relation of [6] that couples the vertical velocity disturbance with the pressure disturbance. In terms of real variables, this relation is written as

$$v_{w,n}(x,t)=p'_w(x,t)\,\mathrm{Real}(A_y)- \\ -\frac{1}{\omega}\frac{\partial}{\partial t}\left(p'_w(x,t)\right)\mathrm{Imag}(A_y) \qquad (2)$$

where $p'_w(x,t)=p_w(x,t)-p_w(x,0)$ is pressure disturbance on the plate surface, A_y is complex quantity characterizing the UAC admittance. For numerical integration, the time derivative of pressure disturbance $p'_w(x,t)$ in (2) is approximated with the second order. The admittance A_y is expressed as

$$A_y=\phi Z_0^{-1}\tanh(\Lambda h)$$

where ϕ is porosity; Z_0, Λ and h are characteristic impedance, propagation constant and depth of an isolated pore, respectively.

Herein the porous coating comprises equally spaced vertical cylindrical blind micro-holes as shown in figure 1. The nondimensional pore radius is $r_0 = 0.333\times10^{-3}$, and the porous layer thickness is $h = 5.5\times10^{-2}$. r_0 and h are made nondimensional using plate length L^*. For this coating, Z_0 and Λ are calculated using the formulas derived in [6]. The UAC boundary condition (1) is imposed in the region $x > 0.3$. Calculations are carried out for porosity $\phi = \pi/16$, which corresponds to the pore spacing $s = 4r_0$. The UAC parameters are chosen so that the number of pores per the disturbance wavelength is approximately 15. Note that the second-mode disturbance wavelength is $\lambda \approx 0.02$ at the frequency $\omega = 260$. It is assumed that the porous surface is aerodynamically smooth and the pore end effects are neglected.

The pressure-disturbance distributions along the solid (figure 2) and porous (figure 3) walls agree satisfactory with LST in the region where the second mode dominates. The porous coating leads to significant decreasing of the disturbance amplification. In the region $x < 0.45$, which is upstream from the instability onset point, the UAC weakly affects the boundary-layer disturbances. The maximum effect is observed in the unstable region, where the porous coating suppresses the second-mode growth rate.

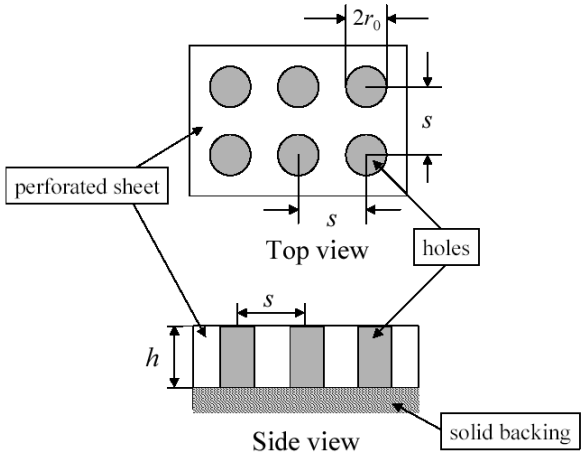

Fig. 1. Porous coating of regular microstructure.

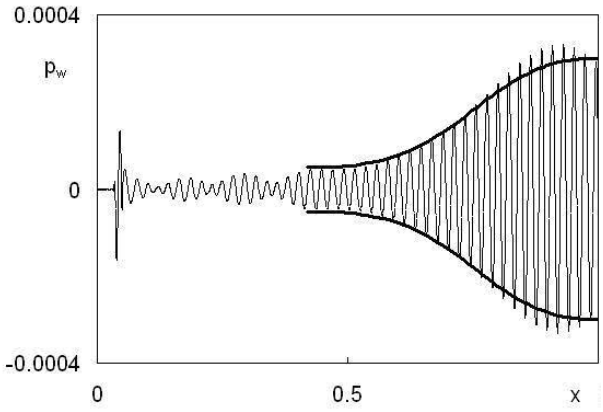

Fig. 2. Pressure disturbances on solid wall; thin line– DNS, bold – LST.

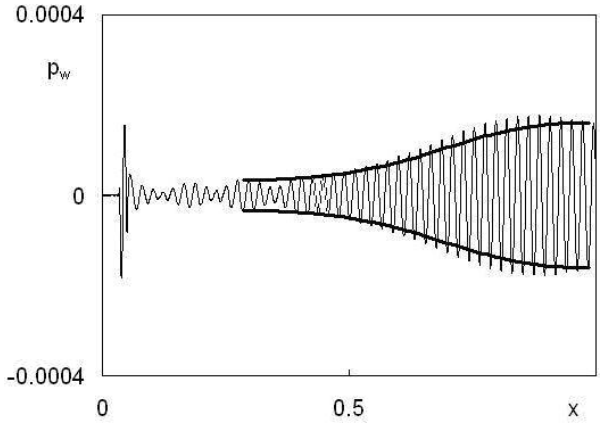

Fig. 3. Pressure disturbances on porous wall; thin line– DNS, bold – LST.

3.2 Sharp cone

DNS of disturbances in the supersonic boundary layer over a sharp cone with apex half-angle 7° is carried out for the flow parameters relevant to the experiments in the ITAM T-326 wind tunnel [6]: $M_\infty = 5.95$, $\mathrm{Re}_\infty = 4.2\times10^6$ is calculated using the cone length $L^* = 350$ mm, $T_w = 6.626$ ($T_0^* = 390$ K, $T_w^* = 0.82T_0^*$), $T_\infty^* = 48.26$ K. The angle of attack is zero.

The computational domain is a rectangle with its bottom side being the cone surface. The computational grid has 4001×151 nodes with clustering in the boundary-layer and leading-edge regions.

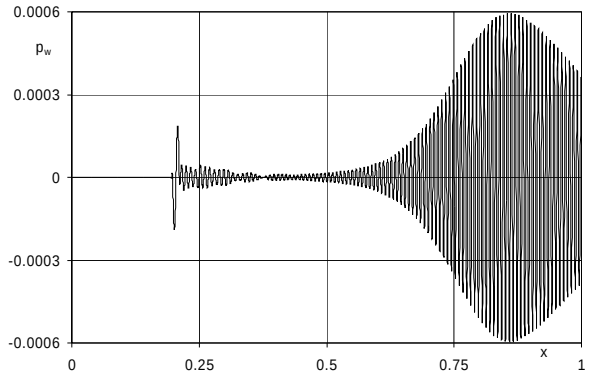

Fig. 4. The wall-pressure disturbance on a sharp cone.

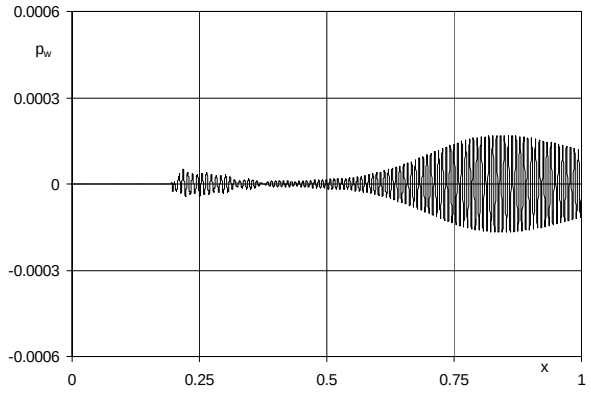

Fig. 5. Pressure disturbance on the cone surface with UAC.

Local periodic suction-blowing was introduced into the flow via the boundary condition (1). The amplitude $\varepsilon = 5\times10^{-4}$ is small enough to meet the LST restriction, $x_1 = 0.1971$, $x_2 = 0.2108$, $\omega = 727.75$ corresponds to the frequency $f^* = 275$ kHz actuated in the experiments [6]. Disturbances of this frequency are relevant to the second-mode instability.

For $x > 0.55$, the boundary-layer mode starts to grow downstream. This is illustrated by the wall pressure disturbance shown in figure 4 at a fixed time instant.

To evaluate the UAC effect on the disturbance field, the porous wall boundary condition (2) is imposed in the region $x \geq 0.52$ (corresponds to $x^* \geq 182$ mm in the experiments [6]). Calculations are performed for the UAC parameters relevant to the

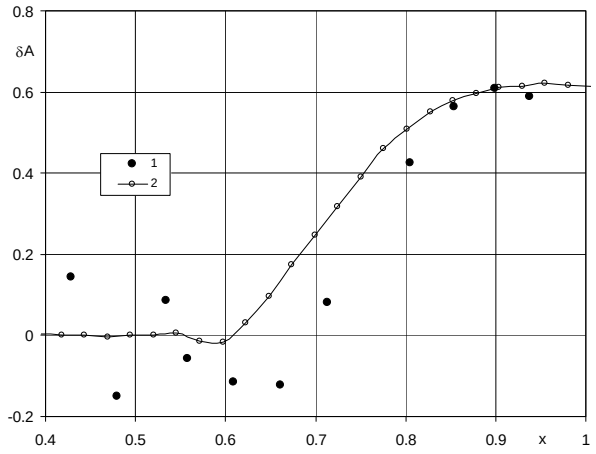

Fig. 6. Relative difference between disturbance amplitudes for solid and porous walls:1 – experiment, 2 – DNS.

experimental conditions: $r_0 = 7.14\times10^{-5}$, $h = 1.286\times10^{-3}$, $s = 4r_0$, $\phi = \pi r_0^2 / s^2 = \pi/16$. For this set of parameters, the pore radius is comparable with the molecular mean free path l^* and the Knudsen number $\mathrm{Kn} \equiv l^* / r_0^* \approx 0.4$ is not small. Therefore, the characteristic impedance Z_0 and the propagation constant Λ in (2) are calculated with the help of method [6] accounting for the rarified gas effect. Figure 5 shows that the pressure disturbance amplitude on the porous wall is essentially smaller than that on the solid wall (figure 4).

Figure 6 compares the data in terms of the relative difference of disturbance amplitude $\delta A = \left(A_s - A_{por}\right)/A_s$, where the subscript "s" ("por") corresponds to the solid (porous) surface. The DNS distribution of this quantity agrees satisfactory with the experiment in the region $x > 0.8$. For $x < 0.7$, where the second mode is not distinguished, the experimental data have a large scatter.

3.3 Compression corner

Consider laminar flow over a compression corner with the inclination angle $\alpha = 5.5^\circ$ (figure 7). Flow variables are made nondimensional using the same procedure as in the previous cases with L^* being a distance

from the leading edge to the corner point. Calculations are carried out for the flow parameters: $M_\infty = 5.373$, $Re_\infty = 5.667 \times 10^6$, $T_\infty^* = 74.194\,K$. The wall temperature is $T_w = 4.043$ ($T_w^* = 300\,K$). Dynamic viscosity μ is approximated using the Sutherland formula. Computational domain is shown in figure 7. The computational grid has 2801×221 nodes (each 20th gridline is shown in figure 7). The grid is obtained by conformal mapping of the upper half plane to the computational domain. The grid nodes were clustered in the boundary-layer and leading-edge regions.

In the corner region, there are compression waves that interact with the boundary layer and induce a recirculation zone (separation bubble). The upper boundary of this zone is approximately a straight line that is typical for supersonic separation (see also figure 8). Downstream from the reattachment point, the boundary layer is thinner than in the upstream vicinity of separation point. Streamlines of the steady-state flow in the separation region are presented in figure 8.

A local periodic suction-blowing is introduced into the flow using the boundary condition (1) with $\varepsilon = 10^{-3}$, $x_1 = 0.0358$, $x_2 = 0.0521$ and $\omega = 450$. An instantaneous distribution of the wall-pressure disturbance is presented in figure 9. In the region $0.6 < x < 0.85$, this disturbance corresponds to the second mode wave. Its wavelength is approximately equal to the doubled boundary-layer thickness. The separation bubble affects the disturbance evolution dramatically. Its amplitude abruptly decreases showing that separation stabilizes the disturbance of considered frequency despite an unfavorable

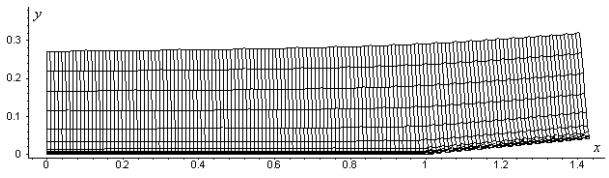

Fig. 7. Computational domain and grid for the case of compression corner.

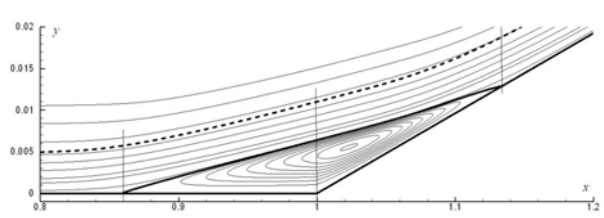

Fig. 8. Streamlines in the separation region; bold line – zero streamline, dashed line – mixing layer boundary.

pressure gradient. Downstream from the reattachment point, the disturbance grows rapidly. This amplification is associated with the second-mode instability.

For modeling of the UAC effect, the boundary condition (2) is imposed on the inclined surface corresponding to $x > 1$. Calculations are performed for the UAC shown in figure 1 with the parameters: pore radius $r_0 = 1.5 \times 10^{-4}$, pore depth $h = 10 \times r_0 = 1.5 \times 10^{-3}$, porosity $\phi = \pi/16$ corresponds to the pore spacing $s = 4r_0$. There are approximately 20

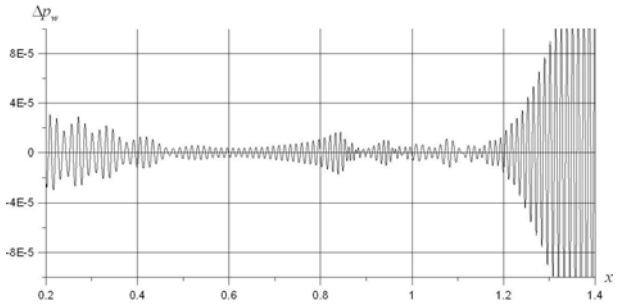

Fig. 9. Pressure disturbance on the solid wall of compression corner.

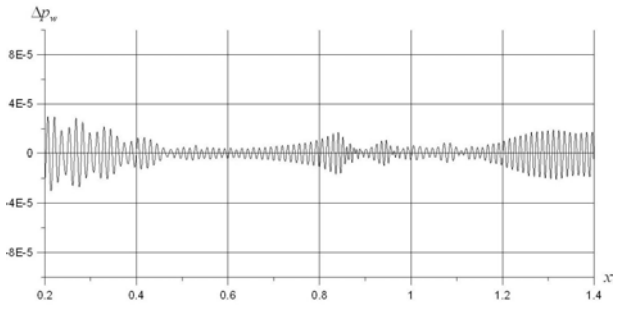

Fig. 10. Pressure disturbance on the porous wall of compression corner.

pores per the disturbance wavelength $\lambda \approx 0.012$. Figure 10 shows the wall-pressure disturbance distribution for the case of porous wall (porosity $\phi = \pi/16$). Comparing this distribution with that on the solid wall (figure 9) we conclude that the UAC weakly affects the disturbance in the separation region $1 < x < 1.2$ and strongly suppresses the second-mode instability downstream from the reattachment point. The porous coating leads to decreasing of the amplitude maximum by a factor of 9.

4 Wavy wall

It was shown in previous section that the amplitude of high-frequency second-mode wave decreases in a separated mixing layer. However there is effective excitation of disturbances downstream from the reattachment point. In this section we discuss results of DNS of disturbances in the near-wall flow over wavy wall with sequence of local separation bubbles. It is expected that this configuration allows us to stabilize the second mode and, at the same time, to minimize growth of disturbances in relatively short regions of the reattached flow.

Calculations are carried out for the flow parameters: $\mathrm{M}_\infty = 5.9$, $\mathrm{Re}_\infty = 1.435 \times 10^6$, $T_\infty^* = 43.08\,\mathrm{K}$. The wall temperature is $T_w = 6.8$ ($T_w^* = 293\,\mathrm{K}$). Dynamic viscosity μ is approximated using the Sutherland formula.

Computations are carried out for flow over a wavy wall with 9 cavities. The surface shape is shown in figure 11 and given by the formula

$$y(x) = \begin{cases} 0, & x < 0.4 \cup x > 1.2 \\ h\left|\cos\left(\pi\left(x - 0.4\right)/0.1\right) - 1\right|, & \\ & 0.4 < x < 1.2 \end{cases}$$

where the groove depth, $h = 0.015$, approximately equals to the doubled boundary-layer thickness (2δ). For the considered flow parameters $\delta = 0.008$ at the station $x = 0.5$ located on the flat plate region.

Computational domain is shown in figure 11. The grid of 2501×241 nodes is obtained by conformal mapping of the upper half plane to the computational domain. The grid nodes were clustered in the boundary-layer.

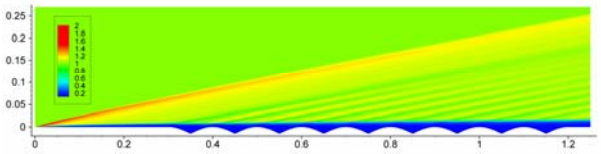

Fig. 11. Density field of steady flow over concave wavy wall.

Density field of the mean flow is shown in figure 11. Wavy surface produces a mixing layer which bridges the cavities and resembles a free shear layer that is almost parallel. It is assumed that such a mixing layer could stabilize the boundary layer disturbances without detrimental effects.

A local periodic suction-blowing is introduced into the flow upstream from the grooved region using the boundary condition (1) with $\varepsilon = 10^{-3}$, $x_1 = 0.05$, $x_2 = 0.087$ and ω varying from 100 to 190.

An instantaneous distribution of the wall-pressure disturbances for the flat plate case and considered free-stream conditions is presented in figure 12 ($\omega = 168$). In the region $x > 0.5$, these disturbances correspond to the second mode waves. For the disturbance of fixed frequency $\omega = 168$, the second mode amplifies and reaches its maximum amplitude at $x = 0.93$. Pressure disturbance on the wavy wall is shown in figure 13. Upstream from the first separation bubble the disturbance behaves like in the flat-plate case. Then it is stabilized over the grooved surface, which transforms the boundary layer flow to the mixing layer bridging neighboring cavities. Further downstream from the last reattachment point, the boundary-layer disturbance behaves as in the flat-plate case.

Comparison of the pressure disturbance amplitude at the station $x = 0.9$ for different frequencies (figure 14) shows that the wavy wall produces stabilization effect in rather wide frequency band $140 < \omega < 190$. DNS shows that the amplitude of high-frequency second mode disturbances can be reduced by the wavy wall

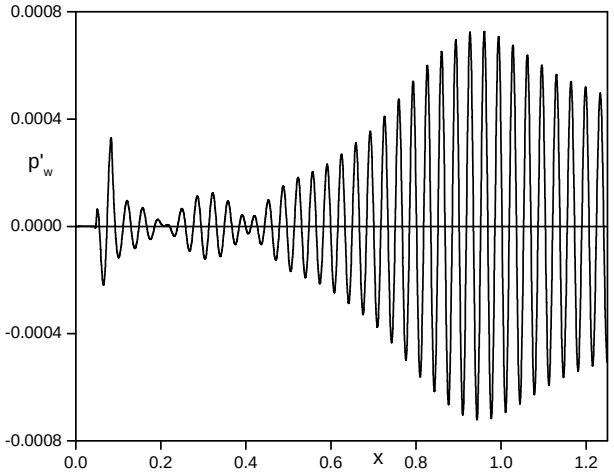

Fig. 12. Pressure disturbance on the flat plate.

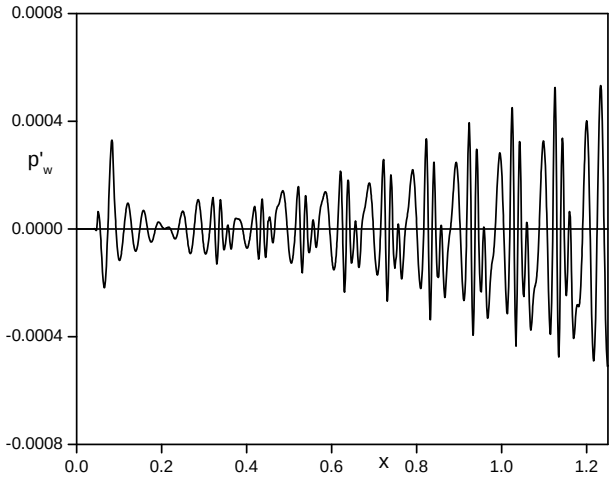

Fig. 13. Pressure disturbance on the wavy wall.

producing a relatively stable free shear layer at sufficiently high free-stream Mach numbers.

5 Conclusions

Two-dimensional direct numerical simulation of supersonic boundary layer stability was carried out for a flat plate with solid and porous walls. A porous coating of regular porosity (equally spaced cylindrical blind micro-holes) effectively diminishes the second-mode growth rate. Particularly the second-mode amplitude decreases twice on the surface covered by the UAC of 20% porosity.

DNS of disturbances on a sharp cone at zero angle of attack was carried out for the cases

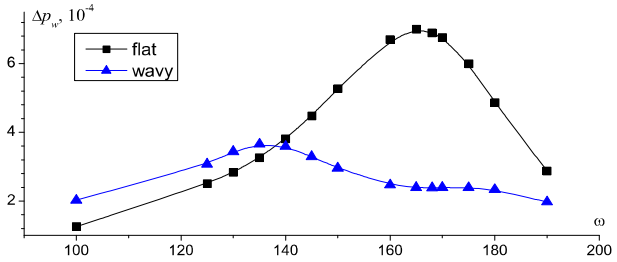

Fig. 14. Pressure disturbance amplitude on the flat plate (black line) and wavy wall (blue line) for different frequencies

with and without UAC. It was shown that UAC diminishes the disturbance amplitude up to four times that agrees with the experimental data.

DNS modeling of disturbance evolution was also performed in a supersonic compression corner flow that comprises a laminar separation bubble. In the solid wall case, high-frequency disturbances associated with the second mode instability are naturally stabilized in the separation region and intensively grow in the reattached boundary layer. The DNS showed that the UAC of regular porosity strongly suppresses the second-mode instability in the reattached boundary layer.

Stability of a separated supersonic near-wall flow over the grooved plate is investigated numerically. DNS shows that the amplitude of high-frequency second mode disturbances can be reduced by the wavy wall producing a relatively stable free shear layer at sufficiently high free-stream Mach numbers.

This work is supported by Federal goal-oriented program “Scientific and scientific-pedagogical personnel of innovative Russia” (state contract No 02.740.11.0154).

References

[1] Mack L.M. Boundary layer stability theory. *Part B. Doc. 900-277*. JPL, Pasadena, California, 1969.

[2] Gaponov S.A., Maslov A.A. *Disturbances Evolution in the Compressible Flows*. Nauka, Novosibirsk, 1980. (in Russian).

[3] Malmuth N.D., Fedorov A.V., Shalaev V.I., Cole J., Khokhlov A.P., Hites M., Williams D. Problems in

high speed flow prediction relevant to control. *AIAA Paper 98-2695*, 1998.

[4] Fedorov A.V., Shiplyuk A.N., Maslov A.A., Burov E.V., Malmuth N.D. Stabilization of a hypersonic boundary layer using an ultrasonically absorptive coating. *J. Fluid Mech*. Vol. 479, pp 99–124, 2003.

[5] Egorov I.V., Fedorov A.V., Soudakov V.G. Direct numerical simulation of disturbances generated by periodic suction-blowing in a hypersonic boundary layer. *Theoret. Comput. Fluid Dynamics*. Vol. 20, No. 1, pp 41-54, 2006.

[6] Fedorov A.V., Kozlov V.F., Shiplyuk A.N., Maslov A.A., Sidorenko A.A., Burov E.V., Malmuth N.D. Stability of hypersonic boundary layer on porous wall with regular microstructure. *AIAA Paper 2003-4147*, 2003.

6 Contact Author Email Address

vit_soudakov@mail.ru

Copyright Statement